Thermal Expansion, Heat Capacity, and Thermal Conductivity of Nickel Ferrite (NiFe[subscript 2]O[subscript 4])

Citation: Nelson, Andrew T., Joshua T. White, David A. Andersson, Jeffery A. Aguiar, Kenneth J. McClellan, Darrin D. Byler, Michael P. Short, and Christopher R. Stanek. "Thermal Expansion, Heat Capacity, and Thermal Conductivity of Nickel Ferrite (NiFe[subscript 2]O[subscript 4])." Edited by M. White. J. Am. Ceram. Soc. 97, no. 5 (April 1, 2014): 1559–1565.

As Published: http://dx.doi.org/10.1111/jace.12901

Publisher: Wiley Blackwell

Persistent URL: http://hdl.handle.net/1721.1/96790

Version: Original manuscript: author's manuscript prior to formal peer review

Thermal Expansion, Heat Capacity and Thermal Conductivity of Nickel Ferrite ($NiFe_2O_4$)

A.T. Nelson[a,*], J.T. White[a], D.A. Andersson[a], J.A. Aguiar[a], K.J. McClellan[a], D.D. Byler[a], M.P. Short[b], C.R. Stanek[a]

[a] *P.O. Box 1667*
Los Alamos National Laboratory, Los Alamos, NM 87545 USA
[b] *P.O. Box 999*
Massachusetts Institute of Technology, Cambridge, MA 02139 USA

Abstract

Nickel ferrite ($NiFe_2O_4$) is major constituent of the oxide formed on the exterior of nuclear fuel cladding tubes during operation, which is comprised of corrosion products. Due to the impact of this oxide layer (typically referred to as CRUD) on the operation of commercial nuclear reactors, $NiFe_2O_4$ has attracted interest. Although advances have been made in modeling CRUD nucleation and growth under a wide range of conditions, the thermophysical properties of $NiFe_2O_4$ at high temperatures have only been approximated, thereby limiting the accuracy of such models. In this study, samples of $NiFe_2O_4$ were synthesized in order to provide the thermal diffusivity, specific heat capacity, and thermal expansion data from room temperature to 1300K. These results were then used to determine thermal conductivity. Numerical fits are provided to facilitate ongoing modeling efforts. The Curie temperature determined through these measurements was in slight disagreement with literature values. Transmission electron microscopy investigation of multiple $NiFe_2O_4$ samples revealed that minor nonstoichiometry was likely responsible for variations in the Curie temperature. However, these small changes in composition did not impact the thermal conductivity of $NiFe_2O_4$, and thus are not expected to play a large role

*Corresponding Author
Email address: **atnelson@lanl.gov**
Telephone: +001/505-667-1268
Fax: +001/505-667-8109

in governing reactor performance.

---

1. Introduction

Nickel ferrite ($NiFe_2O_4$, trevorite) is an inverse spinel[1,2,3], where $8a$ tetrahedral sites are occupied by Fe^{3+} cations $16d$ octahedral sites are equivalently occupied by Ni^{2+} and Fe^{3+} cations. Due to the complex chemical, structural, magnetic and electronic nature of this material, it has been explored for application in spintronics[?] and magnetic storage devices. In addition, $NiFe_2O_4$ is also an important component of so-called CRUD (Chalk River Unidentified Deposit)[5,6,7,8], the oxide scale that forms on the exterior of light water reactor (LWR) components. The formation of CRUD on the upper portions of fuel rods can have significant impact on reactor operation, specifically when present on the upper parts of fuel rods where sub-cooled nucleate boiling occurs. Since these oxide formations have a significantly lower thermal conductivity than the fuel cladding (typically a Zr-based alloy), it is important to understand how the presence of CRUD will impact reactor performance.

The ability to accurately predict fuel surface temperature allows for determination of margin to potential cladding failure due to CRUD-induced localized corrosion (CILC)[9]. Despite this importance, as well as studies on structurally similar oxide compounds (e.g. $MgAl_2O_4$[10]), to our knowledge, no thermal conductivity data exists for $NiFe_2O_4$. The focus of the present work is to provide not only thermal conductivity, but but also the thermal expansion and specific heat capacity data from room temperature through those that would be experienced during a loss of coolant accident (>1300 K)[11,12]. While data covering normal operating conditions (<700 K) is important to facilitate development of compositionally aware software tools aimed at better understanding the formation and growth of CRUD and its impact on nuclear fuel performance[13,14], the latter is vital to development of predictive models to describe reactor conditions during design basis accidents.

This study was conceived to provide the thermophysical properties of $NiFe_2O_4$. In what follows, we present experimental measurements of $NiFe_2O_4$ thermal expansion, heat capacity and thermal diffusivity in order to determine the thermal

conductivity of $NiFe_2O_4$. The results are then analyzed in order to provide numerical fits, as well as interpreted with respect to the Curie temperature (T_C) of $NiFe_2O_4$.

2. Experimental Methodology

The thermal conductivity (λ) of $NiFe_2O_4$ was determined by calculating the product of the thermal diffusivity (D), specific heat capacity (c_P), and density (ρ). Each of these parameters was investigated experimentally through laser flash analysis (LFA, D), differential scanning calorimetry (DSC, c_P), and dilatometry (ρ), respectively. The temperature dependence of the density can be found by applying the thermal expansion curve produced by dilatometry to the room temperature density, which was determined through the immersion measurements previously described.

Although X-ray diffraction (XRD) characterization of the feedstock used for sample fabrication confirmed the absence of other phases, $NiFe_2O_4$ may also exhibit nonstoichiometry. Furthermore, nonstoichometry in $NiFe_2O_4$ is expected to result in only minor variations to the lattice parameter, and thus any deviation from stoichiometry is likely difficult to detect via XRD. Rather, in this study electron energy loss spectroscopy (EELS) and energy dispersive spectroscopy (EDS) were utilized to determine the Fe^{2+}/Fe^{3+} and Ni/Fe ratio of the materials measured to provide at least a qualitative understanding of the degree to which the samples investigated deviated from stoichiometry. Experimental studies have shown that $NiFe_2O_4$ accommodates nonstoichiometry, spinel phases with Fe/Ni ratios above and below 2.0 have been observed [15,16,17,18]. Nevertheless, it is expected that thermophysical properties will vary as a function of deviation from stoichiometry.

2.1. Material Synthesis

The samples characterized in this study were prepared by liquid phase melt mixing followed by conventional cold pressing and sintering. High purity feedstocks of NiO (Puratronic 99.998%) and Fe_2O_3 (Cerac 99.97%) were dried at 473 K in air for 24 hours and then weighed and blended for the required stoichiometry. They were then cold isostatically pressed to 30 MPa to form rods $\approx$ 5 mm in diameter. These rods were fully melted in an optical (halogen) floating

zone furnace, and rapidly cooled in droplet form. The quenched material was then milled in a SPEX mill using a tungsten carbide jar and ball for 20 min. X-ray diffraction confirmed phase pure $NiFe_2O_4$ with a good overall match with the JCPDF database.

Milled materials were sieved (-200 mesh) and cold pressed into 13 mm disks at a pressure of approximately 170 MPa. These disks were then sintered at 1823 K for 2 hours followed by an anneal at 1523 K for 48 hr in air. The as-sintered polycrystalline samples measured slightly over 10 mm in diameter. The thicknesses ranged from approximately 1.5 to 2 mm. The inset of Figure **??** shows images of the $NiFe_2O_4$ pellets that were prepared for thermophysical property measurements.

Porosity is well understood to play a critical role in degrading the thermal conductivity of insulators. While porosity corrections exist and are often employed to normalize data to either very high density or full theoretical density, the accuracy of such models degrade as porosity begins to play a larger role in limiting heat transfer. The goal of this study was synthesis of polycrystalline samples of at least 85% $NiFe_2O_4$ theoretical density (TD). Furthermore, the means used to calculate the thermal conductivity using the LFA technique requires accurate knowledge of the materials temperature-dependent density. The room temperature densities of each sample used in this analysis were determined by immersion density in accordance with ASTM B 962-08[19]. Flourinert FC-43 was used as the immersion fluid, and the measurements were made using a beaker support positioned above the balance pan. The data reported in this work was provided by six samples synthesized as described above. All achieved densities between 89 and 91% TD,

Given the importance of parallel faces to both dilatometry and laser flash analysis (LFA), all samples were lapped by hand using 600 grit (US) SiC papers to obtain a uniform thickness. The samples were prepared to a thickness tolerance no worse than ± 15 microns of the nominal thickness as determined by a vertical micrometer. Samples with the as-sintered diameter were sufficient for LFA measurement, but a smaller diameter was needed for dilatometry and DSC

measurement of heat capacity. An ultrasonic cutter (Model 601, Gatan Incorporated, Pleasanton, CA) and 1 micron SiC abrasive was thus used to section 5 mm discs out of the original 10 mm samples for these measurements.

2.2. Thermophysical Property Measurement

Dilatometry was used to both provide the temperature-dependent density data necessary for calculation of the thermal conductivity as well as the thickness correction for LFA analysis. Measurements were made from room temperature to 1473 K using a pushrod dilatometer (402CD, Netzsch Thermal Analysis, Selb, Germany) equipped with a silicon carbide furnace, alumina fixturing (protective tube, pushrod, and sample supports), and a Type S thermocouple for determination of temperature. The heating rate used for these measurements was 2.5 K/min, and ultra-high purity (UHP) argon was passed over the sample at 100 mL/min. Measurements were made on two separate $NiFe_2O_4$ samples prepared as described above. As a calibration, the thermal expansion of fused silica was measured and found to be within 1% of the data reported in ASTM E228-11[20] and all thermal expansion data was measured per this standard.

Differential scanning calorimetry (404C, Netzsch Thermal Analysis, Selb, Germany) was used to calculate the specific heat capacity of the samples from 313 to 1473 K. A rhodium furnace, platinum head, and type S thermocouples were used in this study. Alumina lined, covered platinum sample pans were used for the baseline, sapphire standard, and sample measurements. Flowing UHP argon was again used, held at a constant flow rate of 20 mL/min. The heating rate was maintained constant at 20 K/min across all three runs. Temperature calibration of the DSC is obtained by comparing the onset of the melting enthalpy of indium, bismuth, aluminum, and gold, each heated at 20 K/min. In each case, the onset deviated less than 0.5 K from the accepted values. The ratio method was utilized to determine the specific heat capacity of the samples using a sapphire standard. The baseline, sapphire standard, and known sample data were collected within a continuous twenty-four hour time interval to minimize deviations in the baseline between runs. Measurements were made on

three separate $NiFe_2O_4$ samples prepared as described above.

Laser flash analysis (427, Netzsch Thermal Analysis, Selb, Germany) was performed using a graphite furnace, alumina sample holders, and a Type S thermocouple for temperature determination. Data was first obtained using a sample prepared as described above and containing a density of 90.6 % TD during cooling from 1573 K to room temperature at 50 K intervals in UHP argon flowing at 100 mL/min. A second sample (91.3 %TD) was used to acquire data at 5 K intervals in the vicinity of T_C. Sufficient overlapping temperatures were included in both runs to evaluate any potential differences in the thermal diffusivity of the two samples, but they produced excellent agreement within 2%. Calibration of the thermocouple used to measure the sample temperature was achieved using T_C of electrolytic iron; the minimum in the diffusivity curve produced was located at 1045.2 K, slightly above the accepted value of 1043 K. As such, an uncertainty of ± 3 K is ascribed to the temperatures of each measurement. Data was obtained in accordance with ASTM E 1461-11 [21], with the exception of the model used for calculation. A Cape-Lehman model was used to calculate the thermal diffusivity based upon the temperature-rise-versus-time data obtained for each shot. No sample coating was used, as the sample surface and optical transport properties were found sufficient for analysis. The laser voltage for all data reported here was 500 V, and the pulse length was 0.5 milliseconds. Three diffusivity measurements were made at each temperature, and the reported thermal diffusivity is the mean of the three calculated values.

2.2.1. Density Functional Theory

DFT calculations of the electronic density of states (DOS) of $NiFe_2O_4$ were performed to compare with the O-K EELS spectra. The Vienna Ab Initio Simulation Package (VASP) [22,23,24] code based on the projector augmented wave (PAW) method [25,26] was used for these calcaultions. Our approach closely follows the study of Fe-Ni-Cr-Zn-O spinel compounds in Ref. [27]. The Perdew-Burke-Ernzerhof (PBE) parameterization of the generalized gradient approximation (GGA) potential [28] was applied for the exchange-correlation potential.

Improved description of the Ni and Fe $3d$ orbitals was achieved by the DFT+U methodology[29,30,31,32]. The Ni U value (U = 5.0 eV for NiO) was taken from[32] and Fe (U = 4.3 eV for tetrahedral and U = 4.0 for octahedral sites in Fe_3O_4) from[33]. The disordered inverse $NiFe_2O_4$ spinel structure as well as the Ni deficient $Ni^{2+}_{0.875}Fe^{2+}_{0.125}Fe^{3+}_2O^{2-}_4$ solid solution were modeled using special quasi random (SQS) structures[34,35], which were constructed to capture the atomic correlation function of random alloys (random distribution of Ni and Fe ions on the respective sublattices)[36]. We used a 56 atom cell for the SQS structures, which was developed by Jiang *et al.* to study inversion in MgX_2O_4 (X = Al, Ga, In) spinels[36]. All calculations applied a plane-wave cut-off energy of 500 eV and a $4\times4\times4$ Monkhorst-Pack k-point mesh[37] with a Gaussian smearing of 0.05 eV. We minimized all structure models with respect to both the volume and shape of the cell as well as atomic positions in order to yield zero external pressure and forces on each atom less than 0.02 eV/Å. The Fe^{3+} ions on tetrahedral sites in the $NiFe_2O_4$ inverse spinel were modeled as anti-ferromagnetically aligned with respect to the both the Ni^{2+} and Fe^{3+} ions on the octahedral sites, which also represents the ground state solution[27].

2.3. Transmission Electron Microscopy

Small fragments of the dense polycrystalline samples whose properties were measured in this study were crushed into a fine powder in air using a SPEX mill in an alumina jar and alumina media. These powders were then suspended into separate alcohol liquid solutions (99.8% min purity) on a copper grid for characterization. The grids were then placed in an oven at 317 K for 15 min to aid in the evaporation of the remaining alcohol and mitigate carbon contamination This technique produced nanoparticle samples measuring approximately 70 nm in diameter.

Experiments were performed on the image-corrected FEI Titan at Los Alamos National Laboratory, operating in diffraction mode at 300 kV and equipped with a Gatan Tridiem electron energy loss image filter. The Titan was used to acquire the O-K, Fe-L, and Ni-L near edge fine structure at $\approx$ 525, 710, and 832

eV respectively with the best achievable spatial and energy resolution for the microscope within a 18 mrad collection half angles giving an energy resolution defined by the full-width half-maximum of the zero-loss peak of 0.83 eV over a 2 second acquisition. The acquisition time to resolve the near edge fine structure was performed over a series of 100 consecutive sub-second exposures taken with a converged beam on the sample. All the spectra were aligned based on their first peak maximum, individually dark count subtracted, and summed to produce the results shown here. The spectra were then processed for their elemental composition, relative valence, and compared with simultaneously acquired EDS.

To analyze the core loss spectra, a fitted Bremsstrahlung background was first removed from all spectra utilizing a standard power law fit. Hartree-Slater modeled K and L-edge atomic cross sections were removed from all O-K, Fe-L, and Ni-L edge spectra, respectively[38]. The effects of plural scattering events were reduced using Fourier-ratio deconvolution[39] by zero-loss deconvolution with a reference low loss spectra. In calculating the elemental abundance, a ratio of the windowed integration over the edge and simultaneous subtracted background noise were utilized to determine the relative abundance of each element in the acquired core-loss spectra[40,41]. To critique the changes in the near edge fine structure, a multiple linear least squares peak fitting algorithm was performed, similar to the method employed by Aguiar *et al.*[42]. To determine the relative valence state of ions at the interface several methods including window-integration and multiple linear peak fitting using the conjugate gradient method[43] were used. In the case of calculating the valence state of the iron, reference Fe-L edge spectra were acquired ranging from 2^+ to 3^+ and the window integration and linear combination least squares technique originally outlined by Cressey *et al.*[44] and later modified by Shao *et al.*[45] and references therein was applied.

3. Results

Data acquired using the techniques described in Section 2.2 are summarized below. As the principle objective of this work is to provide thermophysical property data for $NiFe_2O_4$ suitable for use in CRUD formation and growth codes for nuclear reactor performance modeling, numerical fits are provided in order to readily facilitate such incorporation. The error and relevant temperature ranges of the provided fits is noted in each respective section.

3.1. Thermal Expansion

Figure 1 reports the measured expansion of $NiFe_2O_4$, along with the resulting temperature dependence of the density calculated using the room temperature values for each composition determined by immersion density and the thermal expansion. The thermal expansion (determined through dilatometry as the length change over the initial length, dL/L_0) was converted to a mean linear coefficient of thermal expansion (α), alternatively referenced as a 'technical alpha' in the literature, according to the following equation:

$$\alpha = \frac{(L - L_0)}{L_0(T - T_0)} \tag{1}$$

If the reference temperature for the calculation, T_0, is taken as 298 K, Equation 2 provides α as a function of temperature for $NiFe_2O_4$ as measured in this study:

$$\alpha = (1.6740 \cdot 10^{-5}) - (3.9593 \cdot 10^{-9})T \tag{2}$$

The correlation developed in Equation 2 is valid from 473 to 1273 K, with a recommended error of 3%. The relation reflects the slightly nonlinear expansion of $NiFe_2O_4$ measured in this work. Calculation of a static α over the entire temperate range using a least squares approximation provides $12.9{\cdot}10^{-6}$ K^{-1}. This value matches the experimental data within 5% between 600 and 900 K, but significantly (10-15%) underestimates the measured expansion below this

temperature and slightly (6-8%) overestimates it above. Literature investigations of other ferrite spinels report comparable values between $11{\cdot}10^{-6}$ K^{-1} and $13{\cdot}10^{-6}$ K^{-1} [46,47].

Nickel ferrite was one composition included in a broad matrix of spinels whose thermal expansion and electrical conductivity were investigated by Petric and Ling[48]. They report α of $NiFe_2O_4$ as $10.8{\cdot}10^{-6}$ K^{-1}. However, several other ferrite spinels were investigated along with $NiFe_2O_4$, and all were found to expand at rates between $12{\cdot}10^{-6}$ K^{-1} and $13{\cdot}10^{-6}$ K^{-1}. No experimental details (e.g. heating rate, sample geometry, atmosphere) or sample chemical or structural characterization were provided in the Petric and Ling work, so it is not possible to consider other factors that may be responsible for the lower value they report.

3.2. Heat Capacity

The specific heat capacity data calculated using the ratio method as described above is plotted in Figure 2. The data plotted here is the mean of three different samples. The error is plotted as the larger of the standard deviation among the three or 5%. The latter is ascribed given the accepted accuracy of the ratio method for heat capacity measurement. In addition, $NiFe_2O_4$ c_P data located in the literature is included for comparison. The most prominent feature of the curves are sharp peaks near 860 K, which correspond to T_C of the $NiFe_2O_4$ specimens. The specific T_C values obtained in this work are discussed in Section 4.

The presence of the T_C peak prevents fitting of a single function to the entire temperature range investigated here. Instead, a piecewise model is proposed. At temperatures between 298 and 823 K, the following fit ($R^2 = 0.9986$) estimates the c_P of $NiFe_2O_4$:

$$c_P = -1.2057+(1.1411{\cdot}10^{-2})T-(2.4950{\cdot}10^{-5})T^2+(2.4611{\cdot}10^{-8})T^3-(8.8726{\cdot}10^{-12})T^4 \quad (3)$$

The above fit reproduces the c_P measured in this work and by Ziemniak et al.[49] within 3%. In the regime near T_C, discrete interpretation of the values shown in Figure 2 is suggested. Larger error bars appear in Figure 2 in this region resulting from differences in the DSC curves obtained for the three samples. The data of Ziemniak et al. is slightly higher than the mean values reported[49], but remain encompassed by the error of this measurement.

Finally, for temperatures between 923 and 1373 K, the following curve fit ($R^2 = 0.9867$) is proposed:

$$c_P = -6.5674 + (3.2540 \cdot 10^{-2})T - (5.0578 \cdot 10^{-5})T^2 + (3.3300 \cdot 10^{-8})T^3 - (7.9139 \cdot 10^{-12})T^4 \quad (4)$$

The data of Ziemniak et al. above T_C contains high uncertainties[49]; only data from that study below 1000 K is shown in Figure 2. Data obtained in this work also shows higher error in this regime. As such, an uncertainty of 10% is suggested for Equation 4.

3.3. Thermal Diffusivity

The thermal diffusivity data obtained using LFA is shown in Figure 3. The general trend of the data follows an inverse temperature dependence, but a prominent depression and recovery are visible in the 773-923 K temperature range. The inset of Figure 3 highlights this region. Although we are aware of no previous studies that investigated the thermal diffusivity of $NiFe_2O_4$, limited data for Fe_3O_4 does exist. Magnetite (Fe_3O_4) is also an inverse spinel[50,51], where all Fe^{2+} ions reside on $16d$ octahedral positions, as do half of the Fe^{3+} ions, while the remaining Fe^{3+} ions reside on $8a$ tetrahedral sites. The Curie temperature of Fe_3O_4 is similar to $NiFe_2O_4$, identified as 850 K[52], which is slightly lower than stoichiometric $NiFe_2O_4$. Thermal diffusivity measurements of Fe_3O_4 have identified a similar behavior of D as a function of temperature[53], where a minima occurs at T_C.

3.4. Thermal Conductivity

Finally, the thermal conductivity was calculated as the product of D, c_P, and ρ as reported above. Given the nature of the calculation, it is important to consider propagation of error. The error of each of the three component datasets was included in the thermal conductivity calculation via standard propagation of error. The results are plotted in Figure 4. The data plotted in Figure 4 is corrected to 95% TD using the porosity correction provided by Francl[54] based upon the density of the thermal diffusivity samples. The thermal resistivity (λ^{-1}) is also plotted in Figure 4 in order to better demonstrate behavior as a function of temperature. The thermal conductivity of an insulator is often approximated using Equation 5[55]:

$$\lambda = \frac{1}{A + B \cdot T} \tag{5}$$

where A is a constant that refers to impurity scattering and B is also a constant that refers to Umklapp scattering. Use of this model to fit the experimental thermal conductivity of $NiFe_2O_4$ produced vales of $4.3711{\cdot}10^{-4}$ mK/W and $2.7512{\cdot}10^{-2}$ m/W for A and B, respectively ($R^2 = 0.9985$). This fit is also plotted alongside the experimental data in Figure 4.

4. Discussion

The thermophysical properties measured for $NiFe_2O_4$ exhibit behavior expected of a material where phonon scattering dominates heat transport. Additionally, the dominant feature in both the c_P and D curves are the maximum and minimum, respectively, induced by second order transition that occurs at T_C. However, the product of these values as used to calculate the thermal conductivity results in a continuous thermal conductivity curve that obeys an inverse temperature difference from room temperature to above 1400 K. The T_C indicated by the maximum of the DSC data obtained for the samples synthesized in this work is 864.3 K, with an uncertainty of 0.5 K as dictated by thermocouple calibration. The T_C indicated by the minimum of the LFA data obtained was 863.7 K, with an uncertainty due to the temperature calibration used in the LFA measurement of ± 3 K. These T_C values are slightly larger than the reported literature values of 858 ± 1 K[49,56,57,58,59]. A possible explanation for this discrepancy in T_C is that the samples investigated here had a different nonstoichiometry than samples previously studied. Previously, it has been shown that in other spinels that T_C can be shifted due to cation disorder[60] or cation nonstoichiometry[61].

In order to explore the effect of cation nonstoichiometry on T_C, we have performed similar measurements to those discussed already on different samples synthesized in a separate fabrication run. The second set of samples (referred to as "B," as opposed to "A" which refers to the samples for which results have already been presented) were sintered 100 K lower than sample A (and as described in Section 2), which resulted in 80% TD samples (compared to $\approx$90% for sample A). While these samples were of lower density than desired for the property measurements carried out in this study, they were sufficient to have their T_C accurately measured by the maxima and minima indicated by their DSC and LFA data, respectively. Measurements were repeated using identical methodologies as described above. The DSC and LFA results are plotted in Figure 5, where the c_P and D of Samples A and B are compared. The data

is plotted relative to the value at 800 K in order to emphasize the maxima and minima of the two different parameters as a function of temperature. The absolute thermal diffusivity of Sample B was significantly lower than Sample A owing to the density difference between the samples, but the specific heat capacity values were within the uncertainty of the technique. Interestingly, different T_C values are evident for the different samples, i.e the DSC curve for Sample B indicates T_C of 854.5 K, and the LFA data indicates 854.1 K. These values are accompanied by error bars of 0.5 and 3 K, respectively. The larger error in the LFA data is visible in Figure 5. These values are significantly lower than the values of Sample A, and suggest that the T_C has been shifted from its previous value.

Electron energy loss spectroscopy (EELS) was utilized to analyze both sample A and B to determine if compositional differences between the samples could be responsible for the shift in measured T_C. The EELS samples were prepared from the same material analyzed in Figure 5. Analysis was performed as described in Section 2.3. Figure 6 reports the EELS near-edge fine structure analysis for both samples. Comparing the O-K spectra for Sample A and Sample B, two overall peaks are observed in Figure 6 (a). However, the leading pre-edge indicated as the dashed lined peak 1 is shifted between the two spectra. This behavior suggests a change in the partial density state overlap between the oxygen $2p$ states and transition metal d states, and in particular the presence of Fe^{2+} resulting in a pure chemical shift. The two experimental oxygen spectra are compared to the unoccupied partial density of states for the O $2p$, Ni$3d$, and Fe$3d$ orbitals obtained from the DFT calculations described in Section 2.2.1. The DFT calculations for $Ni_{1-x}Fe_{2+x}O_4$ and $NiFe_2O_4$ reproduce the shift between experimental Samples A and B, respectively. This emphasizes the conclusion that Sample B is Ni deficient and contains excess Fe^{2+} ions.

EELS was also employed to analyze the Fe-L edge spectra for samples A and B in order to resolve any changes in iron valence. By comparing against reference spectra, shown in Figure 6 (b), it can been observed that the expected valence for Sample B differs from Sample A. The origin of the shift in the Fe-L

edge spectra is ascribed to the emergence of Fe^{2+} within $NiFe_2O_4$ in Sample B. That is, Sample B may exhibit Fe-rich non-stoichiometry with Fe^{2+} cations residing on Ni^{2+} sites, which is consistent with the anlysis of the O-K edge spectra.

Energy dispersive spectroscopy (EDS) was also used to characterize the chemical compositions for the two samples. The Fe/Ni ratios determined using EDS were calculated as 1.9 for Sample A and 2.1 for Sample B. First, we note that the EDS result for Sample B appears to confirm the existence of excess Fe, which is consistent with the previously mentioned EELS results. Furthermore, these EDS results also suggest a slight excess of Ni in Sample A.

These results provide a consistent (albeit qualitative) picture of the compositional differences between the samples measured, and therefore the corresponding differences in T_C. That is, the literature value for T_C of $NiFe_2O_4$ is 858K. T_C measured for Sample A was 864 K, which is roughly 8 K larger than the accepted value for $NiFe_2O_4$. It is hypothesized that Sample A, therefore, contained excess nickel. Conversely, Sample B exhibited a T_C of 854K, which is 4 K below the accepted value. The above analysis suggests that Sample B was Ni deficient. It is also worth noting that T_C for Fe_3O_4, magnetite, is 848K. A qualitative trend begins to emerge from this data where T_C decreases as a function of increasing Fe concentration. However, further investigation is required to establish this trend. We also note that the origin of the nonstoichiometry in our samples is unclear, but likely is due to different sintering temperatures.

Finally, it is important to note that while nonstoichiometry seems to influence T_C, λ remains largely unaffected by nonstoichiometry. The plot of thermal resistivity in Figure 4 shows only minor deviation from linearity within the region of the paramagnetic to antiferromagnetic transition, and this deviation is likely attributable to error stemming from use of a steady state technique (LFA) in conjunction with a dynamic measurement (DSC) to determine λ. Calculation of λ using the c_P and D data obtained for Sample B results in a similar trend, although the absolute values are slightly lower due to the higher sample porosity. Since the thermal conductivity of $NiFe_2O_4$ is dominated by phonon transport

(and magnon interactions are minimal), second order magnetic ordering should not be expected to impact thermal conductivity. However, the impact of magnetic ordering on thermal diffusivity is pronounced, and follows naturally from the C_P behavior at T_C. This result has an important implication for CRUD modeling with respect to reactor performance as it is extremely unlikely that the $NiFe_2O_4$ formed is stoichiometric. The result of this work suggests that the thermal conductivity of $NiFe_2O_4$ will remain essentially constant as a function of nonstoichiometry.

5. Conclusions

The thermal expansion, specific heat capacity, thermal diffusivity, and thermal conductivity of $NiFe_2O_4$ were measured from room temperature to 1473 K. The effect of temperature on these properties was, in general, similar to what is expected of an insulating material, with the exception of deviations in c_P and D in the vicinity of the paramagnetic transition. Some of the samples characterized in this work have a Curie temperature slightly higher than the accepted T_C of $NiFe_2O_4$, which was attributed to measured nonstoichiometry. Although the variance in T_C induced by Ni^{2+} on Fe^{2+} sites (or vice versa) has been shown to impact the c_P and D in the magnetic transition regime, the thermal conductivity is not significantly affected since second order magnetic ordering transformations are not expected to impact the phonon transport.

6. Acknowledgments

This work was supported by the Consortium of Advanced Simulation for Light Water Reactors (CASL) program of the US DOE Office of Nuclear Energy.

7. References

[1] E.J.W. Verwey and E.L. Heilmann. Physical properties and cation arrangements of oxides with spinel structures. i. Cation arrangements in spinels. *J. Chem. Phys.*, 15[4]:174-80, 1947.

[2] K.E. Sickafus, J.M. Wills, and N.W. Grimes. Structure of spinel. *J. Am. Ceram. Soc.*, 82[12]:3279-92, 1999.

[3] J.M. Hastings and L.M. Corliss. Neutron diffraction studies of zinc ferrite and nickel ferrite. *Rev. Mod. Phys.*, 25[1]1:114-19, 1953.

[4] U. Lüders, A. Barthélémy, M. Bibes, K. Bouzehouane, S. Fusil, E. Juquet, J.-P. Contour, J.-F. Bobo, J. Fontcuberta, and A. Fert. $NiFe_2O_4$: A versatile spinel material brings new opportunities for spintronics. *Adv. Mater.*, 18:1733-36, 2006.

[5] J. Henshaw, J.C. McGurk, H.W. Sims, A. Tuson, S. Dickinson, and J. Deshon. A models of chemistry and thermal hydraulics in PWR fuel CRUD deposits. *J. Nucl. Mater.*, 353:1-11, 2006.

[6] G.C.W. Comley. The significance of corrosion products in reactor coolant circuits. *Prog. Nucl. Energy*, 16:41-72, 1985.

[7] J.A. Sawicki. Analyses of CRUD deposits on fuel rods in PWRs using Mössbauer spectroscopy. *J. Nucl. Mater.*, 402:124-9, 2010.

[8] W.A. Byers and J. Deshon. Evaluation of fuel clad corrosion product deposits and circulating corrosion products in PWRs. Technical Report 1009951, EPRI and Westinghouse Electric Company, 2004.

[9] J. Deshon. Simulated fuel CRUD thermal conductivity measurements under pressurized water reactor conditions. Technical Report 1022896, Electric Power Research Institute, 2011.

[10] W.D. Kingery, J. Francl, R.L., and T. Vasilos. Thermal conductivity: X, Data for several pure oxide materials corrected to zero porosity. *J. Am. Ceram. Soc.*, 37[2]:107-10, 1954.

[11] G. Schanz, B. Adroguer, and A. Volcheck. Advanced treatment of zircaloy cladding high-temperature oxidation in severe accident code calculations

Part I: Experimental database and basic modeling. *Nucl. Eng. Design*, 232:75-84, 2004.

[12] H.M. Chung. Fuel behavior under loss-of-coolant accident situations. *Nucl. Eng. Tech.*, 37(4):327-362, 2005.

[13] J. Deshon, D. Hussey, B. Kendrick, J. McGurk, and M. Short. Pressurized water reactor fuel CRUD and corrosion modeling. *JoM*, 63:68-76, 2011.

[14] M.P. Short, D. Hussey, B.K. Kendrick, T.M. Besmann, C.R. Stanek, and S. Yip. Multiphysics modeling of porous {CRUD} deposits in nuclear reactors. *J. Nucl. Mater.*, 443(1-3):579-587, 2013.

[15] A. E. Paladino. Phase equilibria in the ferrite region of the system Fe-Ni-O. J. Am. Ceram. Soc., 42(4):168-175, 1959.

[16] H. M. O'Bryan, F. R. Monforte, and R. Blair. Oxygen content of nickel ferrites at 1300C. *J. Am. Ceram. Soc.*, 48(11):577-580, 1965.

[17] A. E. Paladino. Discussion of paper "Oxygen content of nickel ferrites at 1300C". *J. Am. Ceram. Soc.*, 49(5):288-289, 1966.

[18] H. M. O'Bryan, F. R. Monforte, and R. Blair. Reply to discussion of paper "Oxygen content of nickel ferrite at 1300C". *J. Am. Ceram. Soc.*, 49(12):680-681, 1966.

[19] Standard test method for density of compacted or sintered powder metallurgy (PM) products using Archimedes' principle. ASTM International, West Conshohocken, PA, 2008. B962-08.

[20] Standard test method for linear thermal expansion of solid materials with a push-rod dilatometer. ASTM International, West Conshohocken, PA, 2011. E228-11.

[21] Standard test method for thermal diffusivity by the flash method. ASTM International, West Conshohocken, PA, 2011. E1461-11.

[22] G. Kresse and J. Hafner. Ab initio molecular dynamics for open-shell transition metals. *Phys. Rev. B*, 48:13115, 1993.

[23] G. Kresse and J. Furthmüller. Efficiency of ab-initio total energy calculations for metals and semiconductors using a plane-wave basis set. *Comp. Mater. Sci.*, 6:15-50, 1996.

[24] G. Kresse and J. Furthmüller. Efficient iterative schemes for *ab initio* total-energy calculations using a plane-wave basis set. *Phys. Rev. B*, 54:11169-11186, 1996.

[25] G. Kresse and D. Joubert. From ultrasoft pseudopotentials to the projector augmented-wave method. *Phys. Rev. B*, 59:1758-1775, 1999.

[26] P. E. Blöchl. Projector augmented-wave method. *Phys. Rev. B*, 50:17953-17979, 1994.

[27] D.A. Andersson and C.R. Stanek. Mixing and non-stoichiometry in fe-ni-cr-zn-o spinel compounds: density functional theory calculations. *Phys. Chem. Chem. Phys.*, 15:15550-15564, 2013.

[28] J. P. Perdew, K. Burke, and M. Ernzerhof. Generalized gradient approximation made simple. *Phys. Rev. Lett.*, 77:3865-3868, 1996.

[29] V. I. Anisimov, J. Zaanen, and O. K. Andersen. Band theory and Mott insulators: Hubbard U instead of Stoner I. *Phys. Rev. B*, 44:943-954, 1991.

[30] V. I. Anisimov, I. V. Solovyev, M. A. Korotin, M. T. Czyżyk, and G. A. Sawatzky. Density-functional theory and NiO photoemission spectra. *Phys. Rev. B*, 48:16929-16934, 1993.

[31] I. V. Solovyev, P. H. Dederichs, and V. I. Anisimov. Corrected atomic limit in the local-density approximation and the electronic structure of d impurities in Rb. *Phys. Rev. B*, 50:16861-16871, 1994.

[32] S. L. Dudarev, D. N. Manh, and A. P. Sutton. Effect of Mott-Hubbard correlations on the electronic structure and structural stability of uranium dioxide. *Phil. Mag. B*, 75:613-628, 1997.

[33] P. Liao and E. A. Carter. *Ab initio* DFT + U predictions of tensile properties of iron oxides. *J. Mater. Chem.*, 20:6703-6719, 2010.

[34] A. Zunger, S.-H. Wei, L. G. Ferreira, and J. E. Bernard. Special quasirandom structures. *Phys. Rev. Lett.*, 65:353-356, 1990.

[35] S.-H. Wei, L. G. Ferreira, J. E. Bernard, and A. Zunger. Electronic properties of random alloys: Special quasirandom structures. *Phys. Rev. B*, 42:9622-9649, 1990.

[36] C. Jiang, K. E. Sickafus, C. R. Stanek, S. P. Rudin, and B. P. Uberuaga. Cation disorder in MgX_2O_4 (X = Al, Ga, In) spinels from first principles. *Phys. Rev. B*, 86:024203, 2012.

[37] H. J. Monkhorst and J. D. Pack. Special points for Brillouin-zone integrations. *Phys. Rev. B*, 13:5188-5192, 1976.

[38] D. H. Pearson, C. C. Ahn, and B. Fultz. White lines and d -electron occupancies for the 3 d and 4 d transition metals. *Phys. Rev. B*, 47:8471-8478, Apr 1993.

[39] F. Wang, R. Egerton, and M. Malac. Fourier-ratio deconvolution techniques for electron energy-loss spectroscopy (EELS). *Ultramicroscopy*, 109(10):1245-1249, 2009.

[40] R. F. Egerton. Quantitative analysis of electron-energy-loss spectra. *Ultramicroscopy*, 28(1-4):215-225, 1989.

[41] C. Colliex, T. Manoubi, and C. Ortiz. Electron-energy-loss-spectroscopy near-edge fine structures in the iron-oxygen system. *Phys. Rev. B*, 44:11402-11411, 1991.

[42] J. A. Aguiar, Q. M. Ramasse, M. Asta, and N. D. Browning. Investigating the electronic structure of fluorite-structured oxide compounds: Comparison of experimental EELS with first principles calculations. *J. Phys.: Cond. Matt.*, 24(29):295503, 2012.

[43] M. F. Moller. A scaled conjugate gradient algorithm for fast supervised learning. *Neural Networks*, 6(4):525-533, 1993.

[44] G. Cressey, C.M.B. Henderson, and G. van der Laan. Use of L-edge X-ray absorption spectroscopy to characterize multiple valence states of $3d$ transition metals; a new probe for mineralogical and geochemical research. *Phys. Chem. Minerals*, 20(2):111-119, 1993.

[45] Y. Shao, C. Maunders, D. Rossouw, T. Kolodiazhnyi, and G.A Botton. Quantification of the Ti oxidation state in $BaTi_{1-x}Nb_xO_3$ compounds. *Ultramicroscopy*, 110(8):1014-1019, 2010.

[46] I. Kapralik. *Chem. Zvesti*, 23:665-670, 1969.

[47] M. Takeda, T. Onishi, S. Nakakubo, and S. Fujimoto. *Mater. Trans.*, 50:2242-2246, 2009.

[48] A. Petric and H. Ling. Electrical conductivity and thermal expansion of spinels at elevated temperatures. *J. Am. Ceram. Soc.*, 90(5):1515-1520, 2007.

[49] S.E. Ziemniak, L.M. Anovitz, R.A. Castelli, and W.D. Porter. Magnetic contribution to heat capacity and entropy of nickel ferrite ($NiFe_2O_4$). *J. Chem. Phys. Sol.*, 68:10-21, 2007.

[50] E.J.W. Verwey and P.W. Haayman. Electronic conductivity and transition point of magnetite. *Phyisca*, 6(11):979-987, 1941.

[51] M.E. Fleet. The structure of magnetite. *Acta Cryst. B*, 37:917-20, 1981.

[52] L. Néel. Propriétés magnétiques des ferrites: ferrimagnétisme et antiferromagnétisme. *Ann. Phys.*, 3:137-98, 1948.

[53] A.M. Hofmeister. Thermal diffusivity of aluminous spinels and magnetite at elevated temperature with implications for heat transport in earth's transition zone. *Am. Miner.*, 92:1899-1911, 2007.

[54] J. Francl and W.D. Kingery. Thermal conductivity 9: Experimental investigation of effect of porosity on thermal conductivity. *J. Am. Ceram. Soc.*, 37:99-107, 1954.

[55] P.G. Klemens. Theory of heat conduction in nonstoichiometric oxides and carbides. *High Temp.-High Press.*, 17:41, 1985.

[56] E.G. King. Heat capacities at low temperatures and entropies of five spinel minerals. *J. Phys. Chem.*, 60:410-12, 1956.

[57] A.A. El-Sharkawy, A.B. Abousehly, and El-S.M. Higgy. Specific heat capacity, thermal conductivity and thermal diffusivity of spinel ferrite $Ni_{1+2x}Fe_{2-3x}Sb_xO_4$ in the temperature range 400-1000 k. *High Temp. - High Pressure*, 18:265-69, 1986.

[58] N.A. Landiya, G.D. Chachanidse, A.A. Chuprin, T.A. Pavlenishvili, N.G. Lezhava, and V.S. Varazashvili. Determination of the high temperature enthalpies of nickel and cobalt ferrites. *Izv. Akad. Nauk SSSR, Neorg. Mater.*, 2:2050-7, 1966.

[59] G.D. Chachanidze. Thermodynamic properties of nickel and cobalt ferrites. *Izv. Akad. Nauk SSSR, Neorg. Mater.*, 26:376-9, 1990.

[60] J.A. Bowles, M.J. Jackson, T.S. Berquo, P.A. Solheid, and J.S. Gee. Inferred time- and temperature-dependent cation ordering in natural titanomagnetites. *Nature Comm.*, 4:1916, 2013.

[61] Z. Hauptman. High temperature oxidation, range of non-stoichiometry and Curie point variation of cation deficient titanomagnetite $Fe_{2.4}Ti_{0.60}O_{4+\gamma}$. *Geophys. J. R. Astr. Soc.*, 38:29-47, 1974.

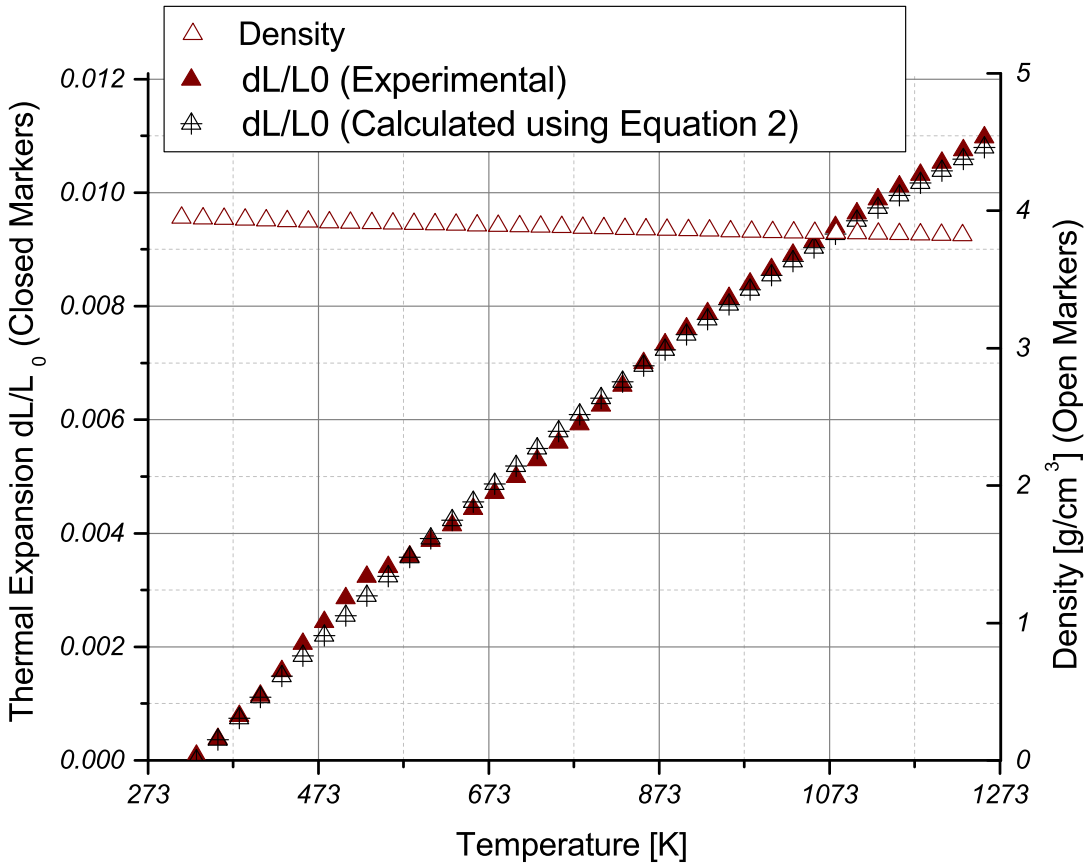

Figure 1: Thermal expansion of $NiFe_2O_4$ determined by dilatometry (left y-axis, closed markers) and the resulting temperature-dependent density (right y-axis, open markers). The thermal expansion as calculated using the correlation proposed in Equation 2 is also plotted.

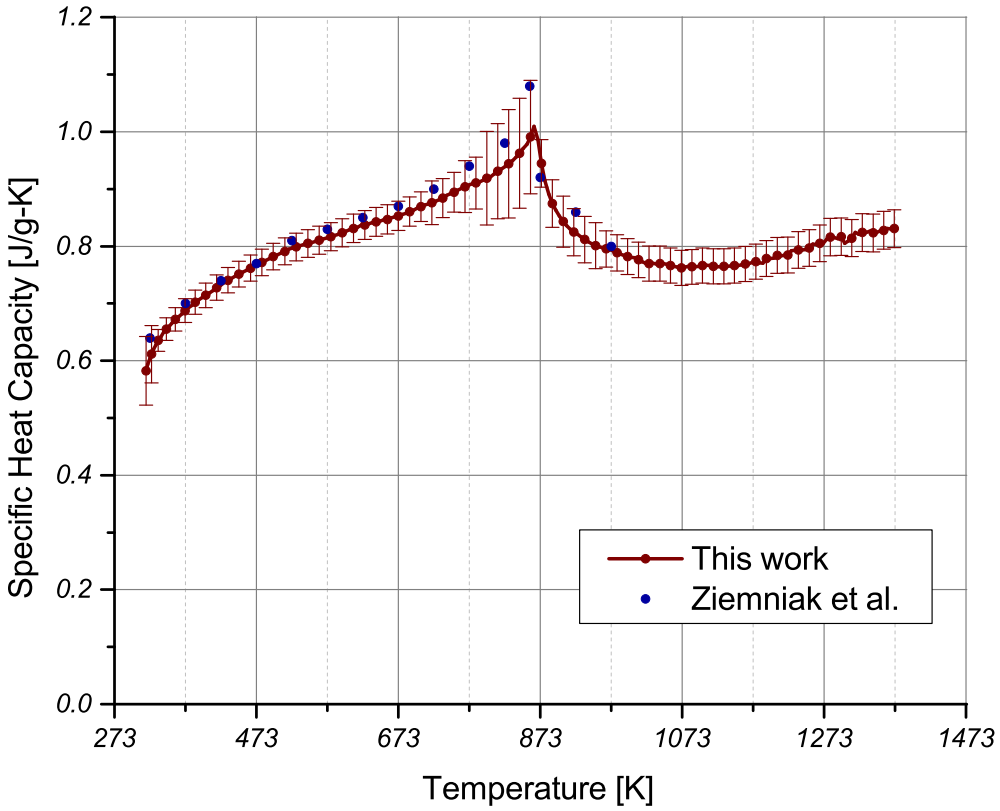

Figure 2: Specific heat capacity of $NiFe_2O_4$ measured using DSC and the ratio method. The data points plotted represent the mean of the heat capacity as calculated for two different samples. Literature heat capacity values for $NiFe_2O_4$ are also included for reference[49].

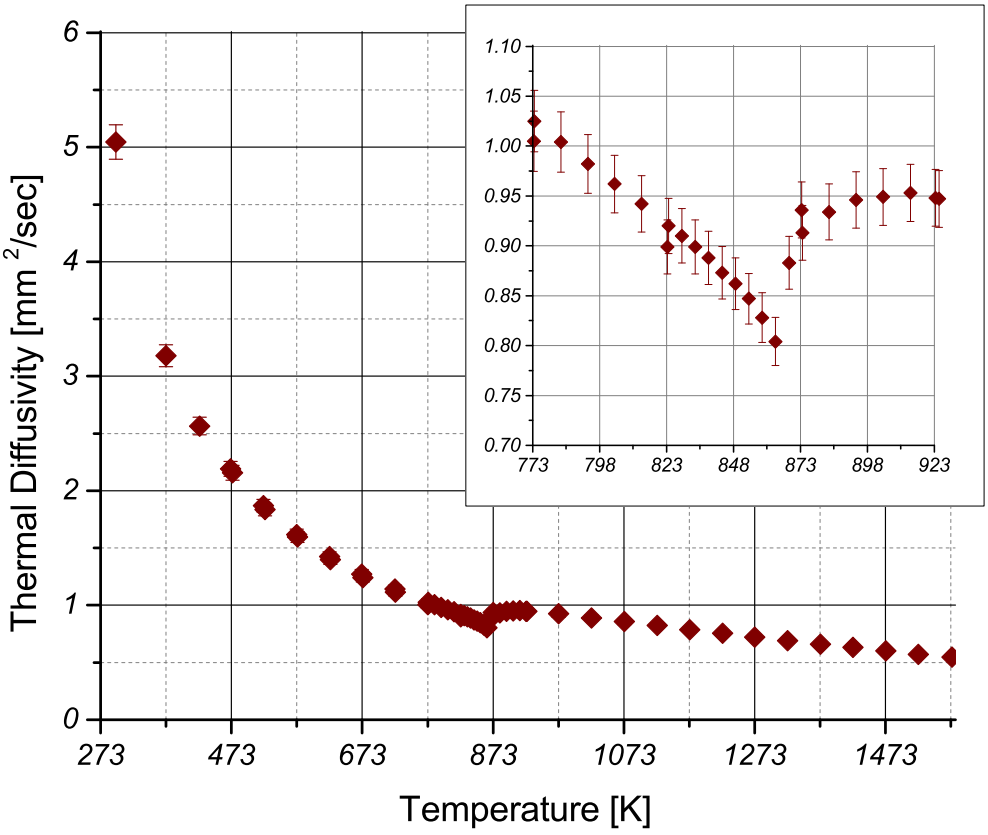

Figure 3: Thermal diffusivity of $NiFe_2O_4$ obtained using LFA. Error bars are included in the figure, but are only visible at low temperatures on this scale. Diffusivity values near the Curie Temperature are shown in the inset, with the minimum observed at 864±3 K.

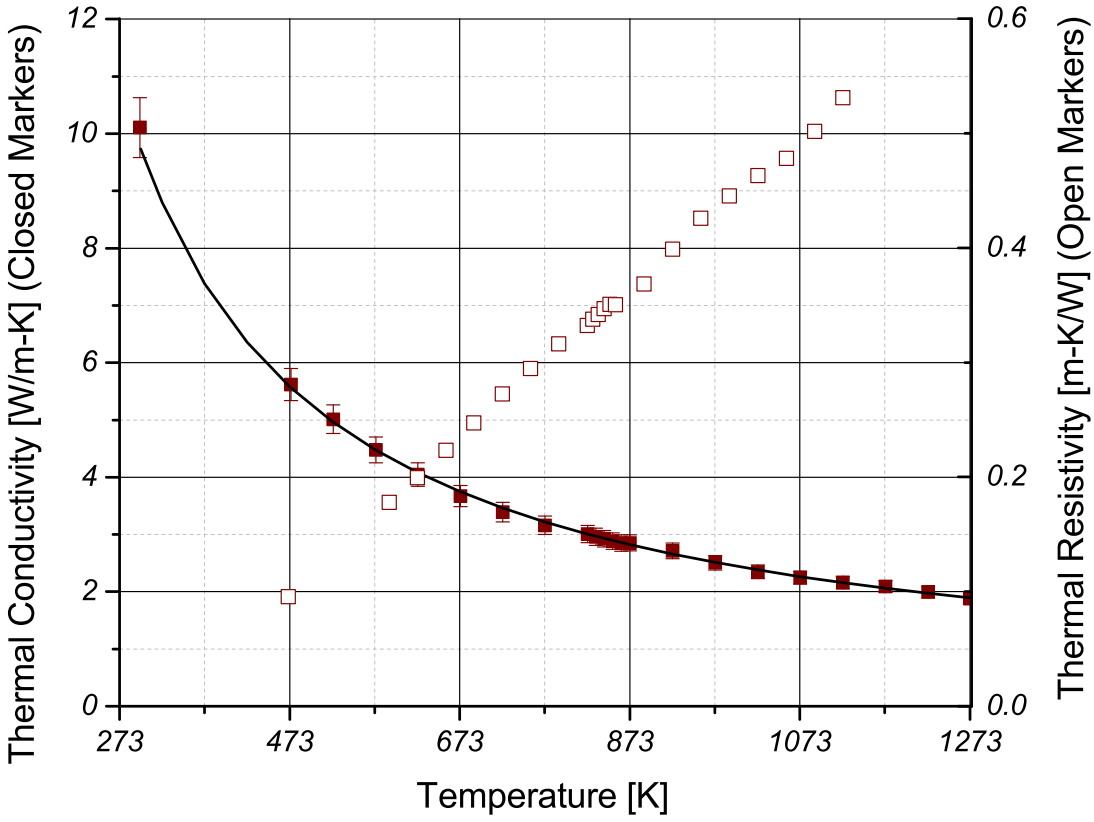

Figure 4: Thermal conductivity of $NiFe_2O_4$ (left y-axis, closed markers), corrected to 95% TD and thermal resistivity (right y-axis, open markers) of $NiFe_2O_4$ as determined in this study. The error bars included for each data point are determined through a propagation of error present in the three individual measurements. The fit provided in Equation 5 with $A = 4.3711 \cdot 10^{-4}$ mK/W and $B = 2.7512 \cdot 10^{-2}$ m/W is also plotted (black line) on top of the experimental data.

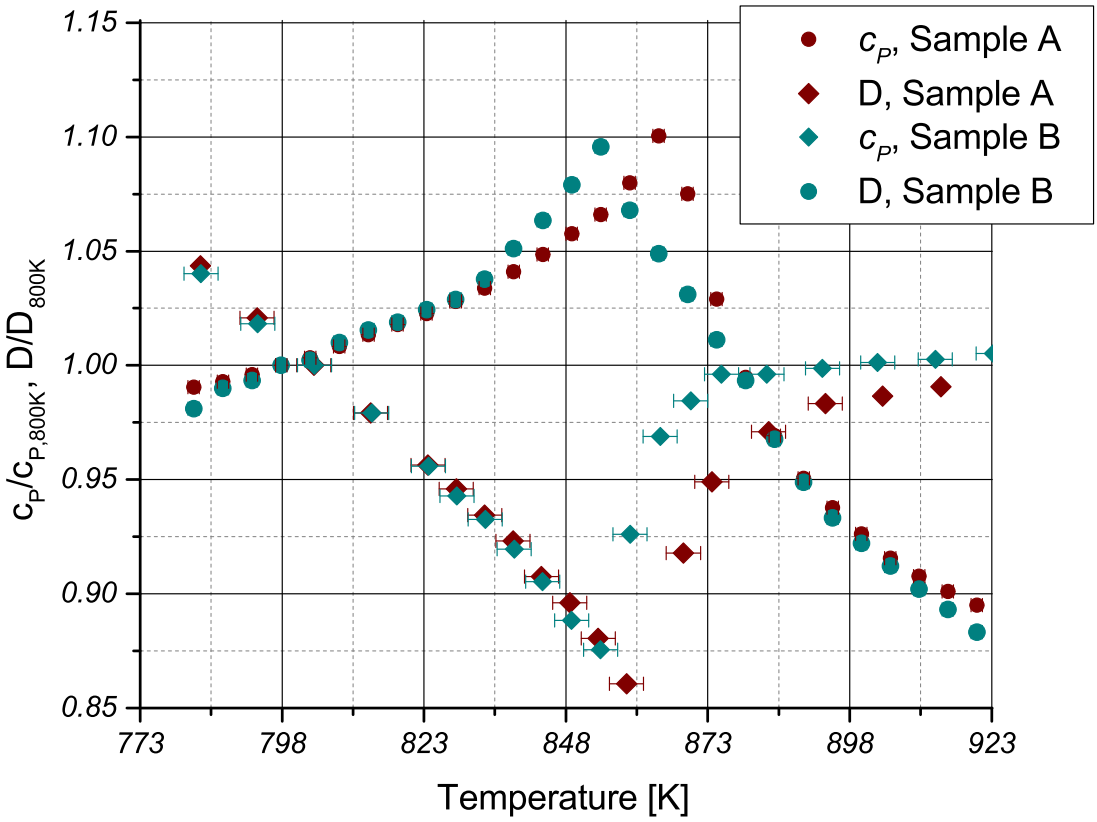

Figure 5: Comparison of the specific heat capacity and thermal diffusivity for $NiFe_2O_4$ samples containing slightly different cation chemistries. All data is normalized to the respective values at 800K. The LFA data is shown with the appropriate error bars indicating the uncertainty in temperature. Similar bars (0.5 K) are plotted on the c_P data, but are not visible at this scale.

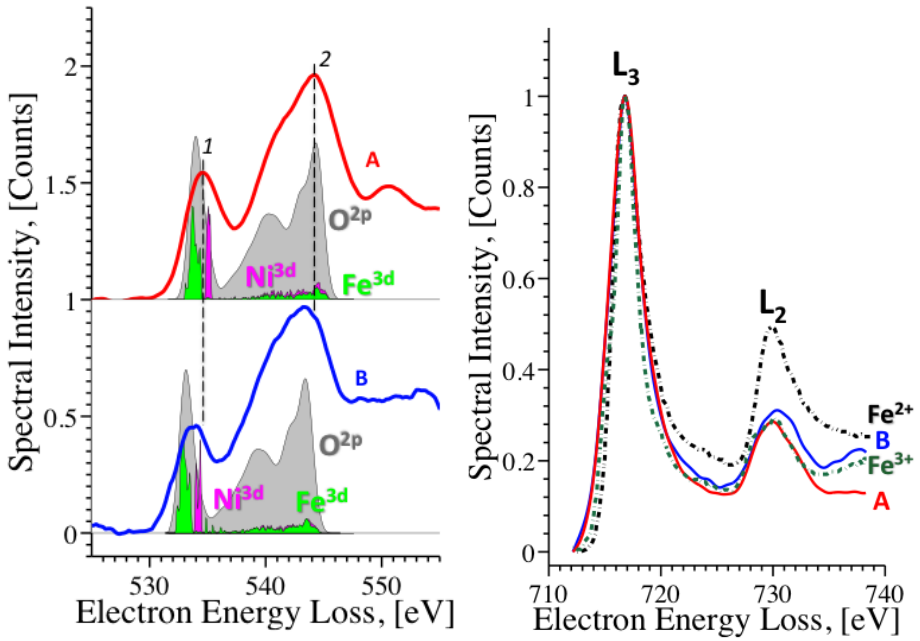

(a) O-K

(b) Fe-L

Figure 6: Averaged O-K (a) and Fe-L (b) core loss edges for multiples of 100 spectra as measured by EELS. A total of 400 spectra were studied and show the same spectral character. For the O-K spectra (a), we have compared spectral profiles for Samples A (top red curve) and B (bottom blue curve) to DFT calculations of broadened unoccupied oxygen p-states (solid gray) and unbroadened partial iron (solid green) and nickel (solid magenta) $3d$-states for nickel ferrite as calculated[27]. In (b), the Fe-L core loss spectra for Samples A (red curve) and B (blue curve) are compared to Fe^{3+} (green dotted curve) and Fe^{2+} (black dotted curve) reference spectra.